

Investigating Moiré Physics in 2D heterostructures using EMPAD detector:

A study of Charge Density Mapping

Sangers, J. (4645197)

Applied Physics - Master Thesis

TU Delft

2nd August 2023

Abstract

Contents

Table of Contents	ii
1 Introduction	1
2 Theory	2
2.1 The Transmission electron microscope	2
2.1.1 Bright Field	3
2.1.2 Dark Field, Z-contrast	3
2.1.3 Energy-dispersive x-ray spectroscopy	5
2.2 TMDC/Crystal structure	5
2.2.1 Transition metal dichalcogenides	5
2.2.2 Crystal lattice and band structure	5
2.2.3 Reciprocal lattice and electron diffraction	6
2.2.4 Convergent beam electron diffraction	7
2.3 Moiré Physics in two-dimensional heterostructures	7
3 Fabrication of two-dimensional moiré heterostructures	8
3.1 Mechanical transfer	8
3.1.1 Exfoliation of monolayer material	8
3.1.2 Assembling a heterostructure	8
3.1.3 Transferring to a TEM grid	9
4 Advanced electron microscopy techniques to map moiré physics at the nanoscale; an electron microscope pixelated array detector.	9
4.0.1 Electron microscope pixel-array detector	9
4.0.2 Strain analysis	10
4.0.3 Ptychography	10
4.0.4 Charge density analysis	10
5 Case study of $MoSe_2/WSe_2$ moiré heterostructures	11
5.1 Verification of moiré pattern and its parameters	11
5.2 Analysis of in-plane strain	11
References	12

1 Introduction

1. use of tmdc, QComp, optoelec
2. flat bands

2 Theory

2.1 The Transmission electron microscope

The Transmission electron microscope (TEM) is a microscope that far exceeds the capabilities of a normal light microscope. Both types of microscope use a series of lenses to magnify the image of a specimen. A normal light microscope can amplify an image up to about $1500\times$ and is limited by the diffraction limit of light. Assuming an average wavelength of 550 nm for green light, a high-end microscope is limited to resolving features 100 nm apart. This limit is insufficient for looking at atomic structures [1].

An electron microscope circumvents this limit by using electrons, not light, to probe the specimen. Electrons when accelerated have a smaller wavelength than light thus allowing for images with resolved features as small as 0.05 nm. [2] The TEM works by releasing electrons from an electron source and accelerating them to an energy typically expressed in kilo-electronvolt; as shown in equation 1, the higher the accelerating voltage of the microscope the smaller the de Broglie wavelength of an electron, which results in a higher resolving power. Modern electron microscopes accelerate electrons up to 300 keV

$$\lambda_e = h \cdot [2 \cdot e \cdot m_e \cdot V_a]^{-1/2} \quad (1)$$

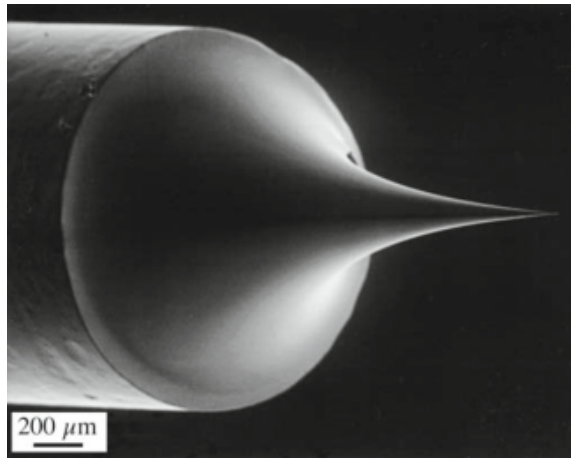


Figure 1: Pictured is the tip of a field emission gun [3]. The tapered tip facilitates the creation of a strongly varying potential that eases the expulsion of electrons from the material. These electrons are then accelerated along the optical axis.

In a TEM the electrons are released from a field emission gun (FEG, pictured in Figure 1). The FEG is placed in proximity to two anodes, the first anode is positively charged to several kilovolts such that it extracts electrons from the tip of the FEG, the second anode is charged to the wanted acceleration voltage [3]. FEGs are about three orders of magnitude brighter than thermionic emission electron sources [4]. After being emitted the electrons pass through a monochromator that reduces the energy spread of the emitted electrons. An electron then continues along the optical axis into an illuminating system consisting of multiple electromagnetic lenses, which lenses are activated and to what extent depends on the operating mode of the electron microscope.

2.1.1 Bright Field

A bright field (BF) image of the sample is acquired by using a parallel electron beam. This beam is formed using the lens configuration shown in figure 2. This parallel beam is typically several micrometers in size at magnifications up to 20k-100k \times . In normal operating mode a BF image is captured by a camera looking at a phosphorous screen or by a camera directly, this method of imaging is most analogous to a normal light microscope. The electron beam is focused in such a way that it illuminates the sample with a parallel beam, such a beam is also used for creating the clearest diffraction patterns.

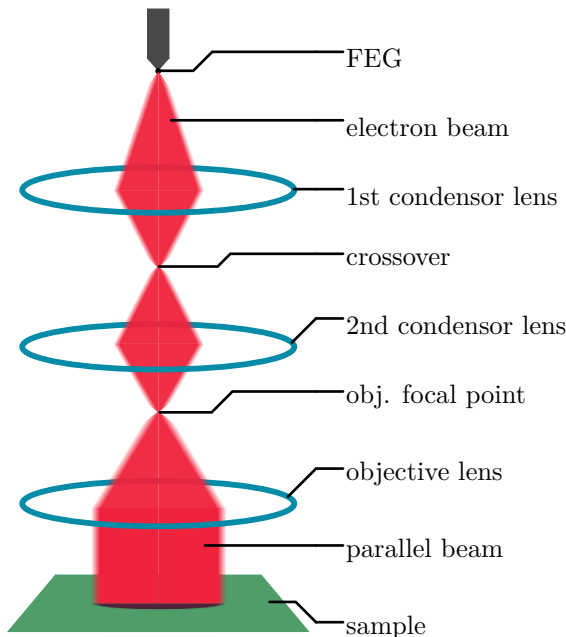


Figure 2: Illumination system for parallel beam.

2.1.2 Dark Field, Z-contrast

For dark field and Z-contrast the electron beam is focused to a small area, this creates a higher intensity electron beam with a probe-like point as can be seen in Figure 3. Since all the electrons are focused on a small area there is no contrast information that can be used to form an image. To form an image using such a beam the probe point needs to be scanned over the sample leading to the term Scanning Transmission Electron Microscopy. Dark field images use electrons scattered away from the optical axis to form an image, to achieve this most STEMs have a series of annular dark field detectors. These ring shaped detectors encircle the central bright field detector and can collect electrons that have been scattered at various angles. Normal dark field detectors collect electrons scattered up to an angle of 50 mrad. The outermost detector is the high-angle annular dark field detector (HAADF) which collects electrons scattered beyond 50 mrad and can be used to create Z-contrast (atomic number Z) or mass-thickness images. The HAADF detector is used since the electrons it collects are almost exclusively incoherently elastically scattered which is proportional to

the atomic number Z . The scanning beam then gathers this atomic number information as intensity information for every probe position in the sample. Layering two monolayers such that the atoms are aligned, and the probe is perpendicularly incident on the sample will sum the intensity of the two atomic weights of the stacked atoms in the image. The stacking pattern can then be determined by looking at a line plot of the atomic mass over atoms.

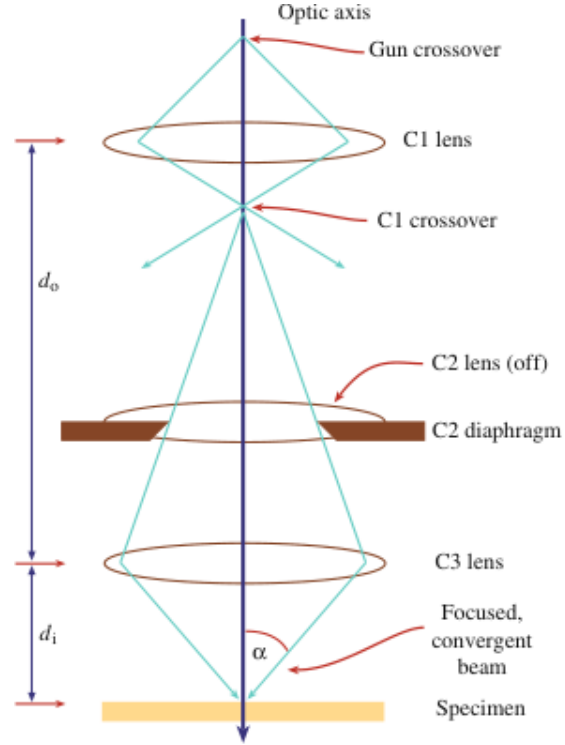


Figure 3: Illumination system for convergent beam.

2.1.3 Energy-dispersive x-ray spectroscopy

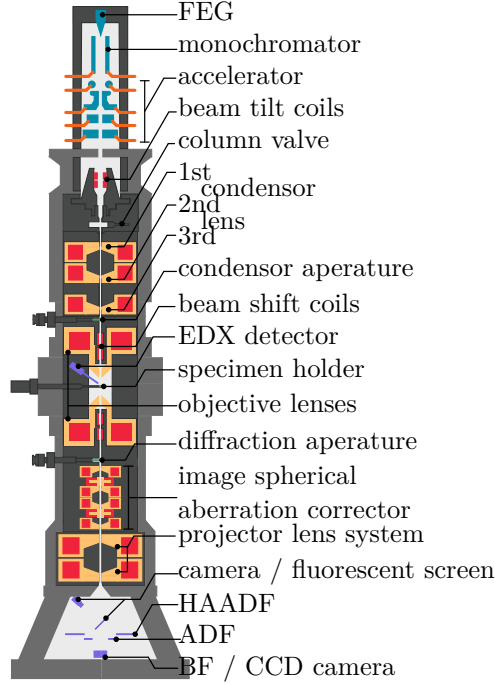


Figure 4: Cross-section of an aberration corrected electron microscope

2.2 TMDC/Crystal structure

2.2.1 Transition metal dichalcogenides

Transition metal dichalcogenides or TMDCs are a family of materials consisting of transition metals (group 3 through 12 on the periodic table) and chalcogen atoms (Sulphur, Selenium or Tellurium) in an MX_2 -configuration, where M is the metal atom and X_2 are the chalcogen atoms [5]. The properties of TMDCs depend greatly on the amount of stacked layers and with individual layers being as thin as 6.5 \AA for MoS_2 these materials are often referred to as layered or two-dimensional materials. Decreasing the amount of layers from bulk changes electrical properties such as the bandgap which for some TMDCs can go from an indirect to a direct bandgap. These electrical properties make TMDCs useful in electronics as transistors and in optoelectronics as emitters and detectors [6, 7, 8]. If present, multiple layers of TMDCs are held together by weak interlayer Van der Waals forces making these materials flexible and transferable using polymer based techniques [9].

2.2.2 Crystal lattice and band structure

An infinitely repeating group of atoms is called an ideal crystal, such a crystal is constructed by attaching the same group of atoms, often called a unit cell, to a lattice. The lattice can be

constructed from n independent lattice vectors. $n = 1$ for an atomic chain, $n = 2$ for a two-dimensional monolayer, and, $n = 3$ for a three-dimensional crystal. If no smaller repeating group of atoms can be constructed to fill the lattice then this group of atoms is called the primitive unit cell and the n -independent lattice vectors are then called the primitive translation vectors a_n [10]. Each of the n lattice vectors signifies a direction and length of displacement needed such that the shifted crystal lattice is indistinguishable from the original crystal lattice. Lattice vectors are also used to specify the orientation of a crystal plane by denoting where the plane intersects the lattice vectors, this procedure allows for unique indexing of crystallographic planes. The use of these planes will be discussed in 2.2.3.

$$\vec{r}' = \vec{r} + u_1\vec{a}_1 + u_2\vec{a}_2 + u_3\vec{a}_3 \quad (2)$$

2.2.3 Reciprocal lattice and electron diffraction

In the previous section the crystal lattice was introduced, and it was mentioned that there were unique planes characterized by the points where they intersect the lattice vectors. In reciprocal space every lattice point is equivalent to one set of these planes. To best understand a crystal, it is helpful to conceptualize it as having two lattices. The first lattice pertains to the organization of the atoms within the crystal's unit cells. The second lattice is a pattern of points that is specific to each crystal and does not correspond to the atom arrangement. Rather, each point in the lattice is linked to a particular set of planes within the crystal [3]. Both lattice constructions are equally valid but are helpful under different circumstances; the reciprocal lattice, for instance, is a useful geometrical construct when talking about diffraction.

The reciprocal lattice, just like the crystal lattice, is constructed by vectors; in the case for the reciprocal lattice these are the reciprocal lattice vectors \vec{b}_n . The reciprocal lattice vectors are constructed from the real-space lattice vectors using equation (3) and satisfy relation (4) with their real-space counterpart. Using these definitions the reciprocal lattice vectors are unique. Any reciprocal vector can now be composed uniquely by a linear combination of the reciprocal lattice vectors, such that any vector is scaled and summed. If the scalars are integers they are the miller indices and correspond to a crystallographic plane.

Scattering off of these planes shows as a series of high-intensity spots in a diffraction pattern image (Figure 5), such an image can be taken in the diffraction mode of a scanning transmission electron microscope (STEM).

$$\vec{b}_i = 2\pi\vec{a}_j \times \vec{a}_k \cdot [\vec{a}_i \cdot (\vec{a}_j \times \vec{a}_k)]^{-1} \quad (3) \quad \vec{b}_i \cdot \vec{a}_j = 2\pi\delta_{ij} \quad (4)$$

In a transmission electron microscope the electrons emanating from the field emission gun are modelled as plane waves. When incident on an atomically thin crystalline sample, the plane waves scatter predictably following the physical criteria that incoming and outgoing electrons beams are plane waves with wave vectors \vec{k}_I and \vec{k}_O for incoming and outgoing waves. The resulting change in wave vector due to the scattering of the sample is then equal to $\vec{K} = \vec{k}_I - \vec{k}_O$. As seen in Figure 6, the outgoing electron beam wavefront is deflected by an angle θ from the incident electron beam such that both are in phase, this angle is the Bragg angle [3]; and using that $|\vec{k}_I| = |\vec{k}_O| = |\vec{K}| = \lambda_e^{-1}$, with λ_e the electron wavelength, the scattering angle can be expressed as:

$$\sin \theta = \frac{|\vec{K}|/2}{|\vec{k}_I|} \quad (5)$$

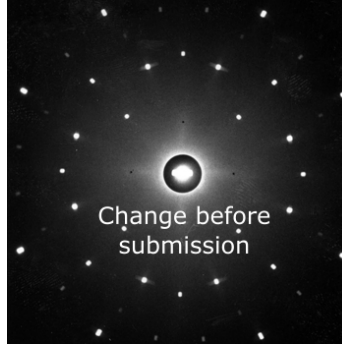


Figure 5: Diffraction Pattern

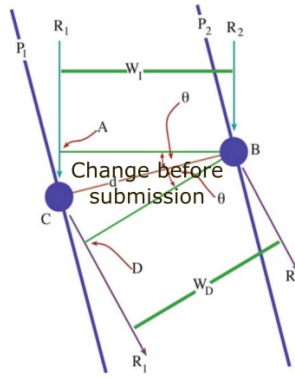


Figure 6: Scattering diagram

If both outgoing rays from the same incoming beam wavefront are then in phase, meaning that the extra distance travelled by one of the rays is a multiple of the wavelength, it shows as a bright spot in the image and then the following condition is met for the Bragg angle:

$$n\lambda_e = 2d \sin \theta_B \quad (6)$$

This shows that scattering allows for a finite quantized momentum transfer from the electron to the crystal lattice or vice versa. In a crystalline sample this results in bright spots in the diffraction image, where each bright spot can be indexed and attributed to a family of planes in the crystal that facilitate the momentum transfer for the electrons to reach that spot on the detector or phosphor film. Just as the real-space lattice has a unit cell so does the reciprocal lattice. In reciprocal space this unit cell is called the Brillouin zone.

2.2.4 Convergent beam electron diffraction

2.3 Moiré Physics in two-dimensional heterostructures

1. moire pattern -> stacking

2. lattice relaxation
3. mini brillouin zone / aligned or antialigned
4. hybridisation, inter/intra transistions and excitons
5. band bending types, umklapp, flat bands

3 Fabrication of two-dimensional moiré heterostructures

3.1 Mechanical transfer

Mechanical transfer in this thesis relates to the practise of both the stamping of two monolayers on top of one-another to form a bilayer heterostructure and the transferring of that heterostructure from the substrate it was stamped on to the holey-carbon TEM grid for inspection in the electron microscope.

3.1.1 Exfoliation of monolayer material

For the preparation of the heterostructures, monolayer flakes were prepared using a three-step process. Firstly bulk crystal material was exfoliated between scotch tape two to three times, using the same method as often is used for graphene [11], to prepare fresh flakes. These fresh flakes would then be transferred to a Polydimethylsiloxane (PDMS) stamp by placing the PDMS stamp on the scotch tape with the flakes before quickly peeling the stamp off with tweezers. For this step it is important that the peeling speed is high as for PDMS the adhesion force to the flake is proportional to the peel-off speed [12]. Thirdly, the flakes present on the PDMS stamp were inspected using an optical microscope before being exfoliated using two PDMS stamps. At this stage PDMS stamps are used for exfoliation as they provide a gentler way of further cleaving the bulk flakes as well as eliminating a further transfer step from tape to PDMS if a monolayer flake were to be exfoliated using tape since stamping on a substrate with tape is difficult. The exfoliation using two PDMS stamps is performed by laying the stamps on another while on a glass slide to provide support after which both stamps are peeled from the glass before separation by two tweezers. Both stamps are now inspected by means of an optical microscope, if monolayer (ML) material is present on either of the stamps it can later be used in creating a heterostructure. If no ML material is present on a stamp the third step can be repeated until there is ML material or the flakes have broken up into unusable small pieces. Furthermore, sacrificial or pristine PDMS stamps can be used to either remove unwanted small flakes or transfer large flakes to a newer and cleaner PDMS stamp, this selective transfer is performed under a microscope such that existing ML material can be avoided as this will likely break if exposed to the force caused by peeling away the sacrificial PDMS stamp.

3.1.2 Assembling a heterostructure

Once two suitably matching monolayer flakes have been located on different PDMS stamps they can be assembled to form a heterostructure. The stamping set-up consists of: a reflective optical microscope, a rotating substrate stage attached to two micromanipulators, and, a stamping stage connected to three micromanipulators. The substrate stage has three degrees of freedom: two micromanipulators control the x - and y -position of the substrate under the microscope and the stage itself is free to rotate to align the edges of the to be stamped ML flakes. The stamping stage

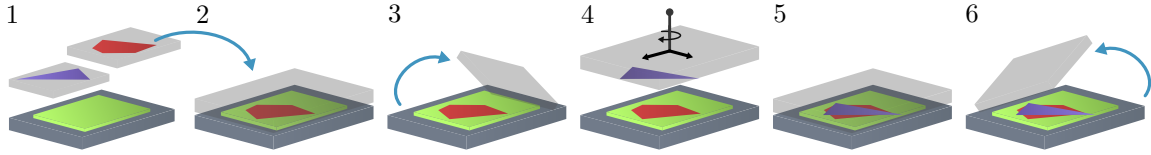


Figure 7: Overview of the global strain present in the heterostructure

is capable of precisely moving a glass slide with a stamp along three axes. The complete stamping set-up is pictured in Figure ?? and is a direct adaptation from previously published set-ups [13, 14]. The ML material is stamped onto the substrate by first adhering the PDMS stamp onto a glass microscope slide and inserting this slide into a holding mechanism on the stamping stage, after which the stamp is carefully brought into contact with the substrate. Since we wish for the flake to adhere to the substrate and not the stamp, we now slowly release the stamp from the substrate. To finish the heterostructure, the last step is repeated for the second flake after having first aligned the ML material on the stamp with that on the substrate.

3.1.3 Transferring to a TEM grid

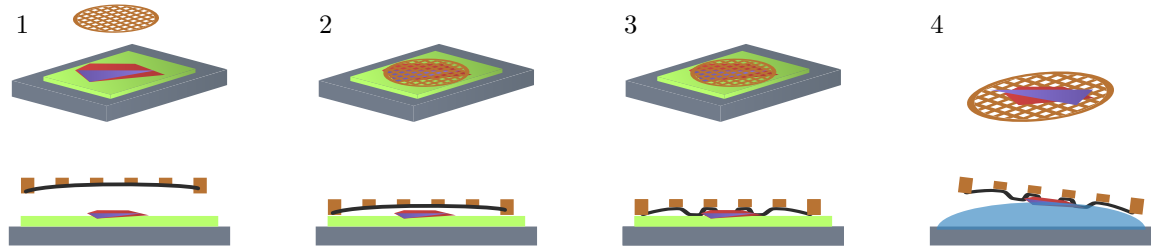


Figure 8: Overview of the global strain present in the heterostructure

4 Advanced electron microscopy techniques to map moiré physics at the nanoscale; an electron microscope pixelated array detector.

4.0.1 Electron microscope pixel-array detector

In a scanning-TEM (STEM) mode the beam is focused to a small probe-like point at the specimen. Elastic scattering then deflects the electrons from the optical axis onto one of the ring shaped detectors encircling the optical axis, these detectors are called the dark field detectors. These singular annular detectors bunch the elastically scattered electrons together, losing valuable information on the exact scattering angle. The electron microscope pixel-array detector (EMPAD) solves this problem by replacing the annular dark field and singular bright field detectors with a single fast-readout, high dynamic range pixel grid on which every pixels' electron dose is stored separately such that after acquisition of a complete STEM scan the bright- and dark-field detectors can be

virtually recreated by integrating the electron dose using annular or circular masks on the data. The pixelated nature of the detector enables the precise computation of the intensity distribution of not only the whole CBED pattern but also within each diffraction disk within the CBED pattern, greatly improving the potential resolution of ptychography methods [15, 16] as well as enabling charge density analysis [17, 18, 19]. A greater accuracy in scattering angle is also available since every pixel in the array has its own smaller range of scattering angles whose electrons the pixel collects.

4.0.2 Strain analysis

4.0.3 Ptychography

4.0.4 Charge density analysis

5 Case study of $MoSe_2/WSe_2$ moiré heterostructures

5.1 Verification of moiré pattern and its parameters

5.2 Analysis of in-plane strain

References

- [1] E. G. van Putten, D. Akbulut, J. Bertolotti, W. L. Vos, A. Lagendijk, and A. P. Mosk, “Scattering lens resolves sub-100 nm structures with visible light,” *Phys. Rev. Lett.*, vol. 106, p. 193905, May 2011.
- [2] C. Kisielowski, B. Freitag, M. Bischoff, H. van Lin, S. Lazar, G. Knippels, P. Tiemeijer, M. van der Stam, S. von Harrach, M. Stekelenburg, and et al., “Detection of single atoms and buried defects in three dimensions by aberration-corrected electron microscope with 0.5-Å information limit,” *Microscopy and Microanalysis*, vol. 14, no. 5, p. 469477, 2008.
- [3] D. B. Williams and C. B. Carter, *Transmission electron microscopy*. New York, NY: Springer, 2 ed., Jan. 2009.
- [4] “Field-emission electron gun, fe electron gun: Glossary: Jeol ltd..”
- [5] A. Eftekhari, “Tungsten dichalcogenides (ws2, wse2, and wte2): materials chemistry and applications,” *J. Mater. Chem. A*, vol. 5, pp. 18299–18325, 2017.
- [6] A. Splendiani, L. Sun, Y. Zhang, T. Li, J. Kim, C.-Y. Chim, G. Galli, and F. Wang, “Emerging photoluminescence in monolayer mos2,” *Nano Letters*, vol. 10, no. 4, pp. 1271–1275, 2010. PMID: 20229981.
- [7] O. Lopez-Sanchez, D. Lembke, M. Kayci, A. Radenovic, and A. Kis, “Ultrasensitive photodetectors based on monolayer MoS2,” *Nature Nanotechnology*, vol. 8, pp. 497–501, June 2013.
- [8] B. Radisavljevic, A. Radenovic, J. Brivio, V. Giacometti, and A. Kis, “Single-layer MoS2 transistors,” *Nature Nanotechnology*, vol. 6, pp. 147–150, Jan. 2011.
- [9] E. C. Regan, D. Wang, E. Y. Paik, Y. Zeng, L. Zhang, J. Zhu, A. H. MacDonald, H. Deng, and F. Wang, “Emerging exciton physics in transition metal dichalcogenide heterobilayers,” *Nature Reviews Materials*, vol. 7, pp. 778–795, May 2022.
- [10] C. Kittel, *Introduction to solid state physics*. Brisbane, QLD, Australia: John Wiley and Sons (WIE), 7 ed., Oct. 1995.
- [11] K. S. Novoselov, Z. Jiang, Y. Zhang, S. V. Morozov, H. L. Stormer, U. Zeitler, J. C. Maan, G. S. Boebinger, P. Kim, and A. K. Geim, “Room-Temperature Quantum Hall Effect in Graphene,” *Science*, vol. 315, pp. 1379–1379, Mar. 2007.
- [12] Y. Kusaka, K.-i. Nomura, N. Fukuda, and H. Ushijima, “Microcontact patterning of conductive silver lines by contact inking and its layer-transfer mechanisms,” *Journal of Micromechanics and Microengineering*, vol. 25, p. 055022, May 2015.
- [13] A. Castellanos-Gomez, M. Buscema, R. Molenaar, V. Singh, L. Janssen, H. S. J. van der Zant, and G. A. Steele, “Deterministic transfer of two-dimensional materials by all-dry viscoelastic stamping,” *2D Materials*, vol. 1, p. 011002, Apr. 2014.
- [14] A. Castellanos-Gomez, M. Buscema, R. Molenaar, V. Singh, L. Janssen, H. S. J. van der Zant, and G. A. Steele, “Deterministic transfer of two-dimensional materials by all-dry viscoelastic stamping,” *2D Materials*, vol. 1, p. 011002, Apr. 2014.

- [15] T. J. Pennycook, A. R. Lupini, H. Yang, M. F. Murfitt, L. Jones, and P. D. Nellist, “Efficient phase contrast imaging in STEM using a pixelated detector. Part 1: Experimental demonstration at atomic resolution,” *Ultramicroscopy*, vol. 151, pp. 160–167, Apr. 2015.
- [16] H. Yang, T. J. Pennycook, and P. D. Nellist, “Efficient phase contrast imaging in STEM using a pixelated detector. Part II: Optimisation of imaging conditions,” *Ultramicroscopy*, vol. 151, pp. 232–239, Apr. 2015.
- [17] J. A. Hachtel, J. C. Idrobo, and M. Chi, “Sub-Ångstrom electric field measurements on a universal detector in a scanning transmission electron microscope,” *Advanced Structural and Chemical Imaging*, vol. 4, p. 10, Dec. 2018.
- [18] Y. Wen, S. Fang, M. Coupin, Y. Lu, C. Ophus, E. Kaxiras, and J. H. Warner, “Mapping 1D Confined Electromagnetic Edge States in 2D Monolayer Semiconducting MoS₂ Using 4D-STEM,” *ACS Nano*, vol. 16, pp. 6657–6665, Apr. 2022.
- [19] S. Fang, Y. Wen, C. S. Allen, C. Ophus, G. G. D. Han, A. I. Kirkland, E. Kaxiras, and J. H. Warner, “Atomic electrostatic maps of 1D channels in 2D semiconductors using 4D scanning transmission electron microscopy,” *Nature Communications*, vol. 10, p. 1127, Mar. 2019.

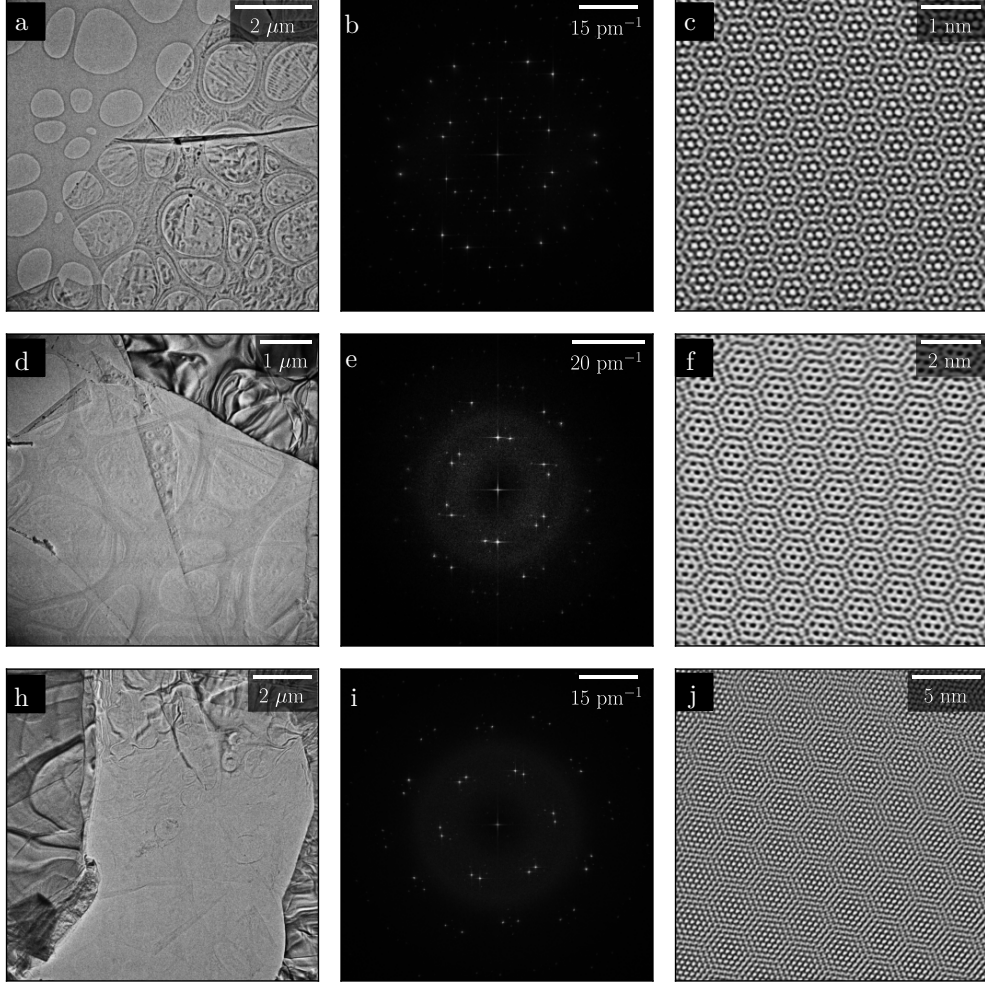


Figure 9: (a, d, h) HR-TEM images of three different $MoSe_2/WSe_2$ -Moiré heterostructures stamped under different angles verified by the FFT of images (b, e, i) taken at $460k\times$ magnification (not shown). The Moiré angle can be determined by measurement of the angle in between the two diffraction peaks in a set, for b, e, i the angle was measured to be 16.6° , 12.2° , and, 8.3° respectively. (c, f, j) displaying a reconstruction of filtered diffraction patterns, showing a clear Moiré superlattice. The Moiré superlattice cell was measured to be 0.47 nm, 1.06 nm, and, 1.69 nm; for c, f, and, j. (a) The two layers of material show a rough surface that seems to arise during or after transfer to the TEM grid.

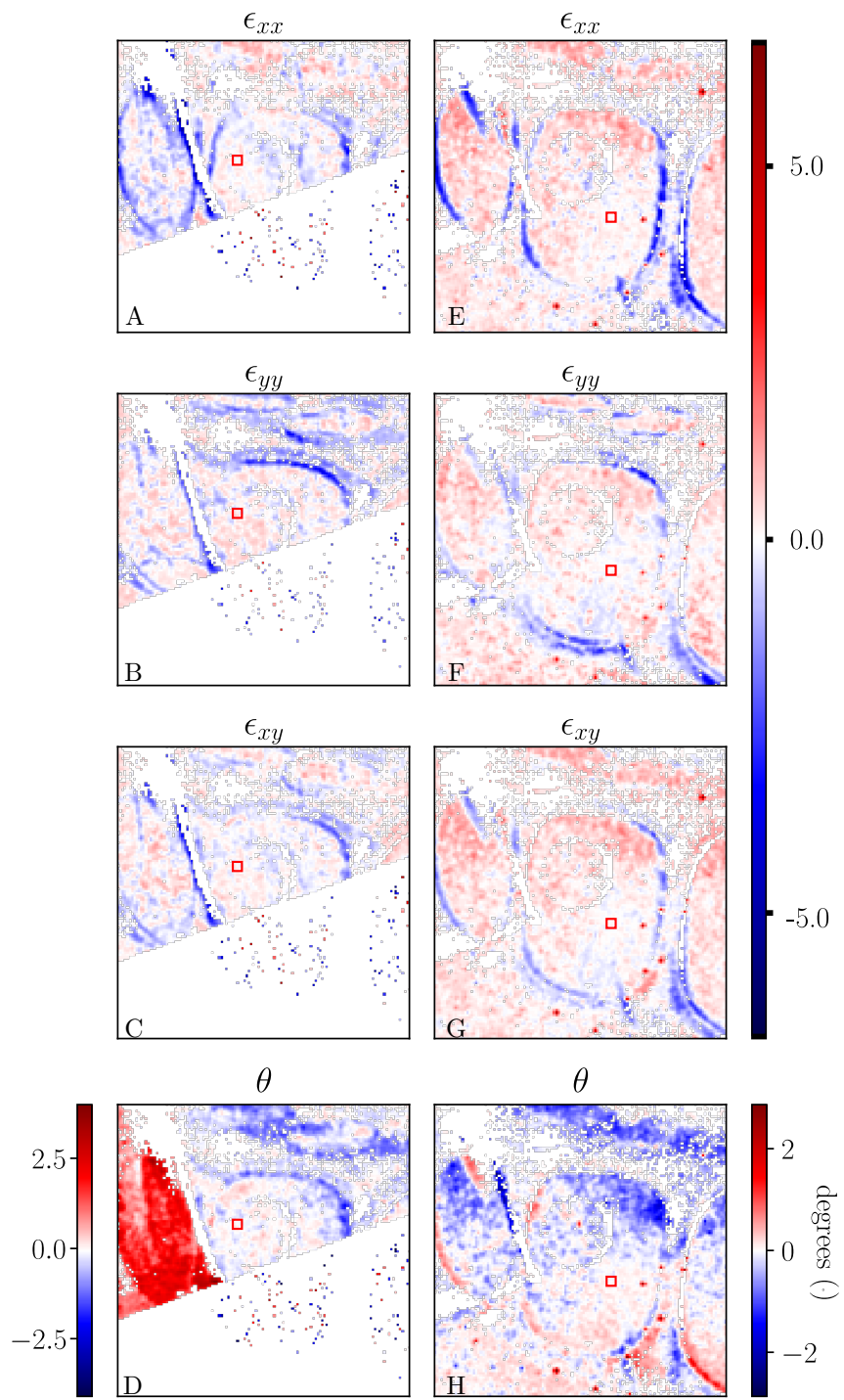


Figure 10: Overview of the global strain present in the heterostructure